

Laser Cladding of Quasi-Crystal-Forming Al-Cu-Fe-Bi on an Al-Si Alloy Substrate

KRISHANU BISWAS, ROLF GALUN, BARRY L. MORDIKE,
and KAMANIO CHATTOPADHYAY

We report here the results of an investigation aimed at producing coatings containing phases closely related to the quasi-crystalline phase with dispersions of soft Bi particles using an Al-Cu-Fe-Bi elemental powder mixture on Al-10.5 at. pct Si substrates. A two-step process of cladding followed by remelting is used to fine-tune the alloying, phase distribution, and microstructure. A powder mix of $\text{Al}_{64}\text{Cu}_{22.3}\text{Fe}_{11.7}\text{Bi}_2$ has been used to form the clads. The basic reason for choosing Bi lies in the fact that it is immiscible with each of the constituent elements. Therefore, it is expected that Bi will solidify in the form of dispersoids during the rapid solidification. A detailed microstructural analysis has been carried out by using the backscattered imaging mode in a scanning electron microscope (SEM) and transmission electron microscope (TEM). The microstructural features are described in terms of layers of different phases. Contrary to our expectation, the quasi-crystalline phase could not form on the Al-Si substrate. The bottom of the clad and remelted layers shows the regrowth of aluminum. The formation of phases such as blocky hexagonal Al-Fe-Si and a ternary eutectic (Al + CuAl_2 + Si) have been found in this layer. The middle layer shows the formation of long plate-shaped $\text{Al}_{13}\text{Fe}_4$ along with hexagonal Al-Fe-Si phase growing at the periphery of the former. The formation of metastable Al- Al_6Fe eutectic has also been found in this layer. The top layer, in the case of the as-clad track, shows the presence of plate-shaped $\text{Al}_{13}\text{Fe}_4$ along with a 1/1 cubic rational approximant of a quasi-crystal. The top layer of the remelted track shows the presence of a significant amount of a 1/1 cubic rational approximant. In addition, the as-clad and remelted microstructures show a fine-scale dispersion of Bi particles of different sizes formed during monotectic solidification. The remelting is found to have a strong effect on the size and distribution of Bi particles. The dry-sliding wear properties of the samples show the improvement of wear properties for Bi-containing clads. The best tribological properties are observed in the as-clad state, and remelting deteriorates the wear properties. The low coefficient of friction of the as-clad and remelted track is due to the presence of approximant phases. There is evidence of severe subsurface deformation during the wear process leading to cracking of hard phases and a change in the size and shape of soft Bi particles. Using these observations, we have rationalized possible wear mechanisms in the Bi-containing surface-alloyed layers.

I. INTRODUCTION

QUASI-CRYSTALLINE materials were discovered in 1984 by Dan Shechtman *et al.*^[1] to herald a new era in crystallography and atomic architecture of solids. A few years after the rush of the initial discovery, a few laboratories started looking at the properties of these materials and, thereby, exploring the possibility of the potential use of these materials. Quasi-crystalline materials are characterized by the long-range order without translational periodicity featuring noncrystallographic symmetry. The aperiodic arrangement of atoms in the lattice leads to several distinctive properties, such as very high hardness,^[2] low friction coefficient,^[3] low thermal conductivity,^[4] low surface energy,^[5] high corrosion and oxidation resistance,^[6] *etc.* These properties make them potentially useful in many applications. However, due to their low room-temperature ductility,^[7] these materials are often

not found suitable for bulk applications. An attractive alternative is to use these materials in the form of coatings on soft metals and alloys, such as aluminum and Al-Si alloys.

The Al-Cu-Fe system is known to be a stable quasicrystal-forming system.^[8] This ternary system has been extensively studied due to the possibility of a number of applications in the form of coatings.^[9] However, their brittleness at room temperature and complex solidification pathways have made it difficult to use them. Therefore, it is important to study the effect of the addition of other elements on the morphological modifications of icosahedral phase-forming Al-Cu-Fe alloys. The quaternary addition of Si to this system significantly influences the phase formation. According to Lee *et al.*,^[10] an Si addition up to 5 at. pct leads to an increase of the volume fraction of icosahedral phase in the microstructure. A further increase of Si content from 9 at. pct to 15 at. pct leads to the formation of the 1/1 cubic rational approximant to the icosahedral phase. These approximant phases are crystalline in nature with quasi-crystalline motifs and can be derived from the rational cut of six-dimensional hyper-space of the icosahedral quasi-crystals. Therefore, they have similar properties to those of the parent quasi-crystalline phases. According to Quivy *et al.*,^[11] the cubic rational approximant phase exists over a large domain of compositions and temperatures, sometimes in coexistence with the

KRISHANU BISWAS, Graduate Student, and KAMANIO CHATTOPADHYAY, Professor, are with the Department of Metallurgy, Indian Institute of Science, Bangalore-560012, India. Contact e-mail: kamanio@met.iisc.ernet.com ROLF GALUN, Scientist, and BARRY L. MORDIKE, Emeritus Professor, are with IWW, Technical University, Clausthal, D-38678, Clausthal-Zellerfeld, Germany.
Manuscript submitted May 31, 2004.

icosahedral phase. These authors have pointed out that the structural change from icosahedral phase to rational approximant can occur if the Si content in the quaternary alloy is more than 2 at. pct. The quinary addition of Bi is expected to yield nano-sized Bi particles in the final microstructure, because Bi is immiscible to each component of the quaternary alloy. Thus, rapid cooling through the miscibility gap can lead to the formation of Bi particulates of various shapes and sizes. The low hardness of this phase (termed, henceforth, as soft phase) may enhance the mechanical and tribological properties of the composite coating.

Laser cladding has been extensively used to obtain wear- and corrosion-resistant coatings on different substrates.^[12] The process involves the formation of a coating by melting the desired material, along with a thin layer of substrate, with a high-power laser beam normal to the surface. The coating forms due to rapid solidification of the melt with materials build-up on the substrate. The laser cladding can be a single-step or two-step process. In the former case, coating material is fed into the melt pool created by the laser beam in the form of powder, paste, or wire, while in the latter case, the coating material is predeposited on the substrate and, subsequently, remelted by the laser beam. The predeposition of the coating materials can also be done by a laser cladding process. Our study aims at developing coatings of quasi-crystalline and related intermetallic compounds of the Al-Cu-Fe-Bi alloy containing Bi dispersions by laser cladding using an elemental powder mixture of Al, Cu, Fe, and Bi on Al-10.5 at. pct Si alloy substrates. In addition, the present study attempts to correlate the microstructure with properties such as hardness, friction, and wear, with particular emphasis on the influence of the Bi distribution in the microstructure to the properties.

II. EXPERIMENTAL DETAILS

Clad layers were prepared using a continuous-wave CO₂ laser (Rofin Sinar model R10000) with a peak power of 10 kW. The laser was focused 30 cm above the focal point to get a beam size of about 2.5 mm. This results in a broad intensity distribution that does not lead to vaporization and, thus, is well suited for cladding. The initial experiments of cladding were done with 3 kW power to get clad layers with good adherence to the substrate and uniformity along the surface. The clad layers were then remelted at higher traverse speeds to simulate different growth conditions. The processing conditions used are as follows: laser power, 3 kW; focus, 30 cm out of focus; diameter of beam, 2.5 mm; carrier gas flow rate, 4 L/min; and powder feed rate, 4 g/min.

An elemental powder mixture of aluminum, copper, and iron, with the nominal composition Al₆₅Cu_{23.3}Fe_{11.7}, was used. In the mixture, Bi powder was added to an amount not exceeding 10 wt pct of the total powder. The basic advantage of using elemental powder mixtures as compared to the alloyed powder is that the cost incurred is much less in using an elemental powder mixture. Therefore, although difficulties exist in the control of the compositions of the clad layers, we have adopted and standardized this route. The inductively coupled plasma (ICP) technique has been used to determine the approximate composition of the clad layer. The desired powder composition was obtained by mechanically mixing elemental

powder. The particle size of the powder was between 25 and 100 μm . The Al-10.5 at. pct Si alloy was used as a substrate. The substrate movement was controlled by a numerically controlled X-Y table under the stationary laser beam. The various sets of scanning and remelting speeds was obtained by controlling the linear motion of the substrate. In order to get uniform roughness, the substrates were sandblasted in all cases prior to the cladding experiments. An argon jet was used to shield the melt pool from oxidation. The coatings were prepared by a two-step laser cladding process. The scan rate used for cladding was 300 mm/min. The subsequent remelting experiments were done employing scan rates of 300, 500, 1000 and 1200 mm/min.

Structural analysis of the clads was performed using a JEOL* X-ray diffractometer (JDX-8030) with Cu K_{α} ($\lambda =$

*JEOL is a trademark of Japan Electron Optics Ltd., Tokyo.

1.5402 \AA) radiation. The microstructural investigations were performed using an optical microscope (Olympic brand), a JEOL JSM 840A scanning electron microscope (SEM), and a JEOL 2000FXII transmission electron microscope (TEM). The local phase composition was determined using the SEM (operated at an accelerating voltage of 20 kV) by standardless energy-dispersive spectroscopy (EDS) X-ray analysis (Oxford brand) on polished and etched sections. Numerous composition-analysis examinations of well-equilibrated samples using EDS in the SEM have shown that the scattering of the measured compositions is in the range of 1 at. pct. This scattering follows from the precision of the method rather than from a compositional variation of the studied materials. Therefore, the precision of the compositional measurements presented in this article is limited by ± 1 at. pct. Three independent measurements of elemental composition of different phases have been made to get statistics of the compositional data. The average of the three values at each position is used to obtain the composition profile of constituent elements. The hardness profiles of the clad layers were measured using a Shimadzu 2000 microhardness tester with a load of 25 g. A minimum number of five indents were made per location to obtain good statistical representation of the dataset. In each case, the average of all the measurements was used to get the hardness plot for each track. The error bars represent the maximum and minimum value in each data set. The sliding-wear tests were carried out with a pin-on-disk configuration using a friction and wear monitor (model TR-201EV, supplied by Ducom). The following parameters were used for this purpose. Sample size, $4 \times 4 \times 10$ mm; track radius 34 mm; disc velocity, 0.89 m/s; loads, 0.5, 1, 1.5, and 2 kg; duration of test, 5 minutes; and level of vacuum, better than 10^{-5} torr.

Prior to the sliding-wear-testing, the pins were polished under water with 1200-grade emery paper, followed by standard alumina and diamond polishing. All the wear tests were carried out on a disc of 11 cm in diameter and 8 mm in thickness, made up of EN-24 steel with a hardness of HRC 54.

III. RESULTS

We have studied various process parameters for optimization of the surface alloying process. We shall only present here the detailed results of two representative and

optimized samples processed under two different conditions, namely, the as-clad condition, with a scan rate of 300 mm/min (powder feed rate of 4 g/min), and the as-clad and remelted condition, with remelting done with a scan rate of 500 mm/min. In both cases, laser power used was 3 kW. The results of the two cases will be presented separately.

A. Characterization of the As-Clad Sample

The as-clad and remelted layers obtained in our experiments are quite thick (about 2 mm). Thus, the X-ray diffraction patterns from the surface will contain information only of the surface and not across the depth of the surface-alloyed layer. Such a phase analysis of the as-clad and remelted samples has been carried out. The X-ray diffraction pattern of the as-clad samples reveals the presence of a 1/1 cubic rational approximant phase of icosahedral quasi-crystal co-existing with monoclinic $\text{Al}_{13}\text{Fe}_4$, tetragonal CuAl_2 , and Bi.

In order to characterize the laser-processed layer completely, detailed microstructural and phase analyses have been carried out using the optical microscope, SEM, and TEM. The results of these investigations will be presented next.

A low-magnification optical micrograph covering half of the cross section of the as-clad layer is shown in Figure 1(a).

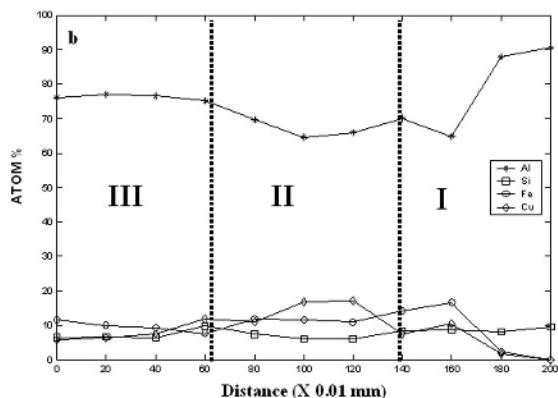
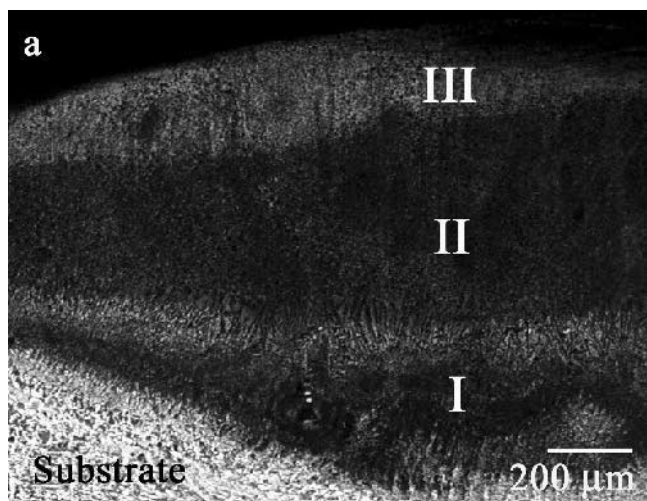


Fig. 1—(a) Low-magnification optical micrograph of half of the cross section of the as-clad sample, showing three different microstructural layers labeled as I, II, and III. (b) Composition profiles showing the variation of elemental compositions as a function of distance in the three layers.

Three distinct microstructural regions, from the bottom (near the substrate) to the top, can be identified and are labeled as I, II, and III. The composition analysis using EDS of the clad layer reveals elemental compositions in three different regions (Figure 1(b)). The elemental compositions vary substantially along the height of the clad layer. One can observe that the aluminum content (90 to 70 at. pct) is quite high near the clad/substrate interface, while the iron content is also on the higher side (>10 at. pct). The copper content in this layer remains below 10 at. pct, and the silicon content is found to remain at an almost constant level of 8 at. pct. In layer II, the aluminum content decreases, but the copper content increases to about 18 at. pct. There are dips in the iron and silicon content in this layer. The top layer (III) shows a substantial increase in the aluminum content (>75 at. pct). Both the copper and silicon content show a substantial drop compared to layer II, while the iron content remains at about 10 at. pct.

Scanning electron microscopy observations of the as-clad layer reveal the presence of different phases and morphologies. All the SEM images shown are taken in backscattered electron (BSE) imaging mode to clearly depict the compositional contrast and, thereby, the different phases. Figure 2(a) shows a representative BSE micrograph of the region near the substrate corresponding to region I marked in Figure 1(a). In addition to the primary aluminum dendrites ($\alpha\text{-Al}$) with dark contrast and a well-developed faceted phase (referred henceforth as blocky phase “B”), the micrograph clearly reveals the lamellar nature of the eutectic region (marked as eutectic) in the interdendritic regions and the dispersion of bismuth particles. Different facets of blocky phase in one of the particles are shown by white arrows. Measurements of angles between the sharp facets show the angle to be close to 120 deg. The EDS spectra taken from this phase reveal the composition to be $\text{Al}_{63.8}\text{Si}_{8.4}\text{Fe}_{18.6}\text{Cu}_{9.2}$.

In order to reveal the nature of the eutectic, the sample was deeply etched. The inset in Figure 2(a) shows a typical higher-magnification BSE image of the eutectic region. The observed contrast indicates that the eutectic contains three phases with dark, gray, and light contrast. The composition of the eutectic regions as determined by EDS indicates a ternary composition close to $\text{Al}_{62}\text{Si}_6\text{Cu}_{32}$. Therefore, we can conclude that the observed eutectic is a ternary one consisting of long, platelike CuAl_2 (light contrast), needle-like silicon (gray contrast) and α -aluminum (dark contrast). All the phases are marked on the micrograph.

The SEM micrograph corresponding to the middle of the clad region (marked II in Figure 1(a)) is shown in Figure 2(b). The microstructure is dominated by a phase that has a long, plate-shaped morphology (marked P in the micrograph). A light-contrast phase (α_H) having a dendritic morphology coexists in the space between the plates. The interdendritic regions exhibit a dark contrast. Fine particles of Bi (with bright contrast) are distributed throughout this region. A careful examination reveals that most of these particles are located near the interfaces between the P and α_H phases.

Figure 2(c) shows the BSE micrograph corresponding to the top portion of the clad layer (marked III in Figure 1(a)). The micrograph shows the presence of a number of phases. A long, plate-shaped phase (P) is present in this micrograph. Along with these, one can find the presence of starlike

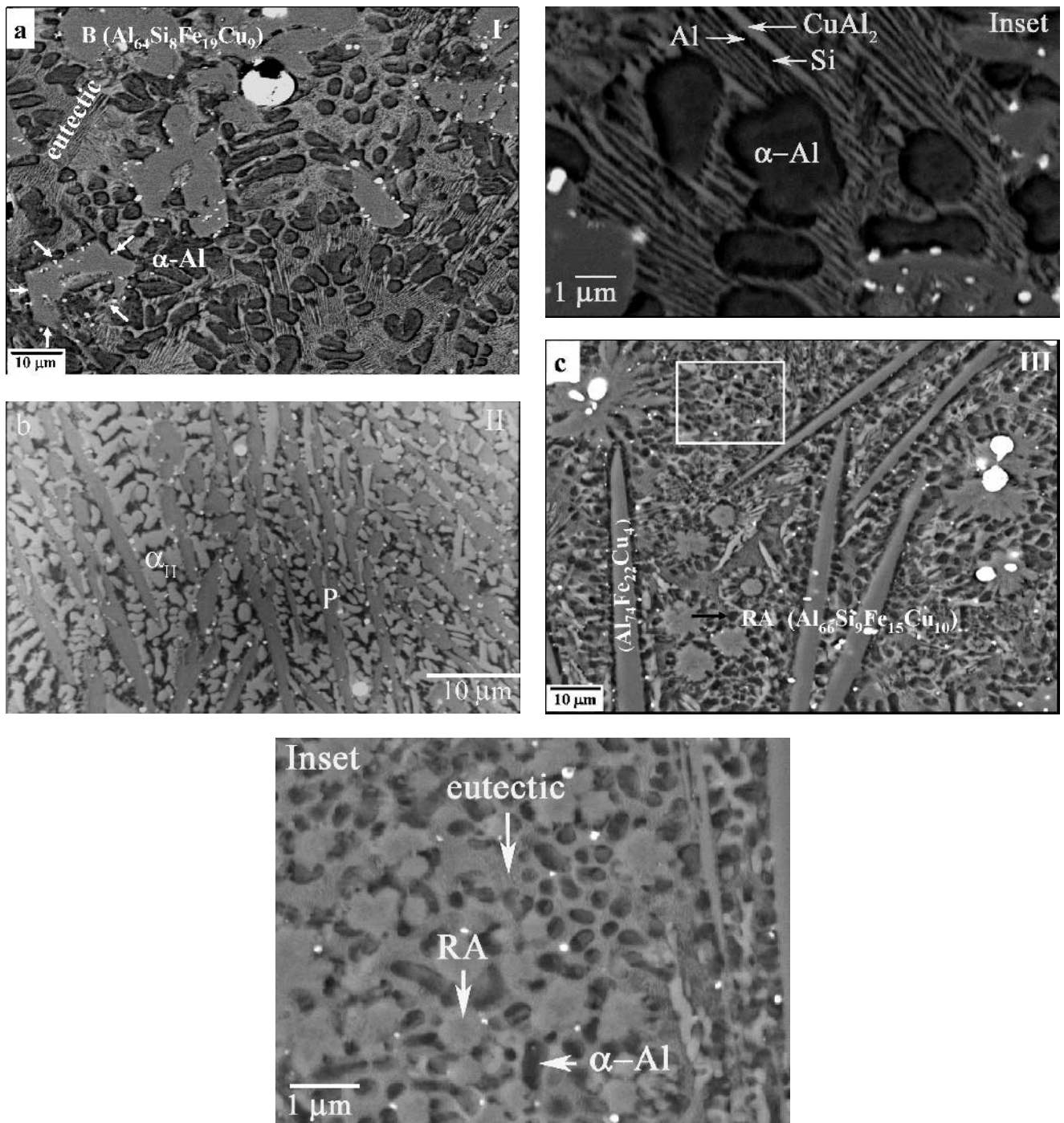


Fig. 2—(a) High-magnification BSE image of region I (as marked in Fig. 1(a)), showing different phases: blocky (B phase) α_{II} -AlFeSi, α -Al, and a eutectic. The B phase is found to be faceted. The facets are of one such crystal, shown by a white arrow. The inset shows a ternary eutectic consisting of CuAl_2 , α -Al, and Si. (b) High-magnification BSE image of region II from Fig. 1(a). (c) High-magnification BSE image of region III from Fig. 1(a). The inset provides a higher-magnification BSE image showing a fine-scale microstructure of the region, marked by the white box. Different phases are marked in the figures. Refer to the text for details.

dendrites (the rational approximate) as well as regions with a fine-scale microstructure consisting of primary α -Al and eutectic (Figure 2(c), inset). The EDS taken from these star-like dendrites shows that these dendrites have the composition of $\text{Al}_{66}\text{Si}_9\text{Fe}_{15}\text{Cu}_{10}$, whereas the composition of the plate-shaped phase is found to be close to $(\text{Al,Cu})_{13}\text{Fe}_4$. The EDS analysis indicates that the composition of the eutectic is close to $\text{Al}_{61}\text{Si}_2\text{Cu}_{34}\text{Fe}_3$.

In order to obtain more structural information, a detailed TEM characterization was carried out. We have focused our attention on regions II and III, as these regions are believed to have greater influence on the properties of the surface-alloyed layer. Figure 3(a) shows a low-magnification bright-field TEM micrograph of the region corresponding to region II in Figure 1(a). One can observe that the micrograph reveals the existence of three phases. These phases are marked on

the micrograph as long, platelike $\text{Al}_{13}\text{Fe}_4$, $\alpha\text{-Al}$, and a eutectic. The plate shaped phase exhibits a faulted morphology, and this leads to a diffuse streaking in the selected-area dif-

fraction pattern (SADP) shown in Figure 3(c). A dark-field image using streaks reveals the faults, as shown in the inset. The SADPs from the plates can be indexed in terms of a

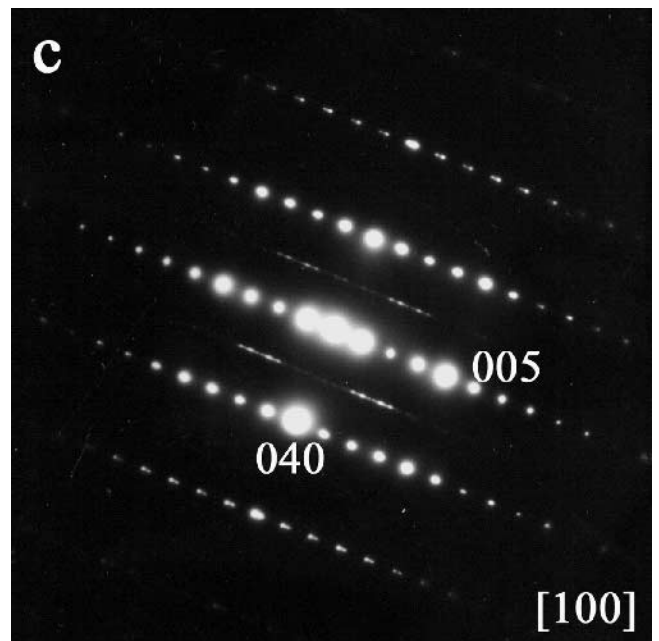
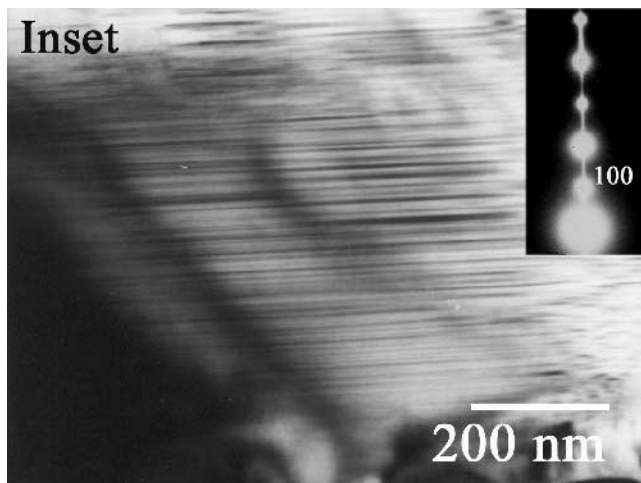
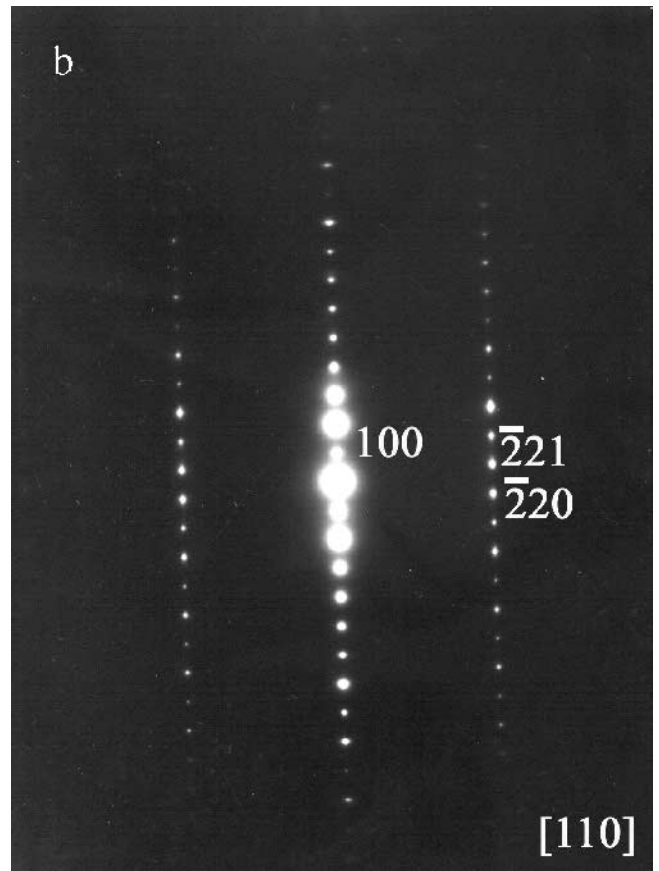
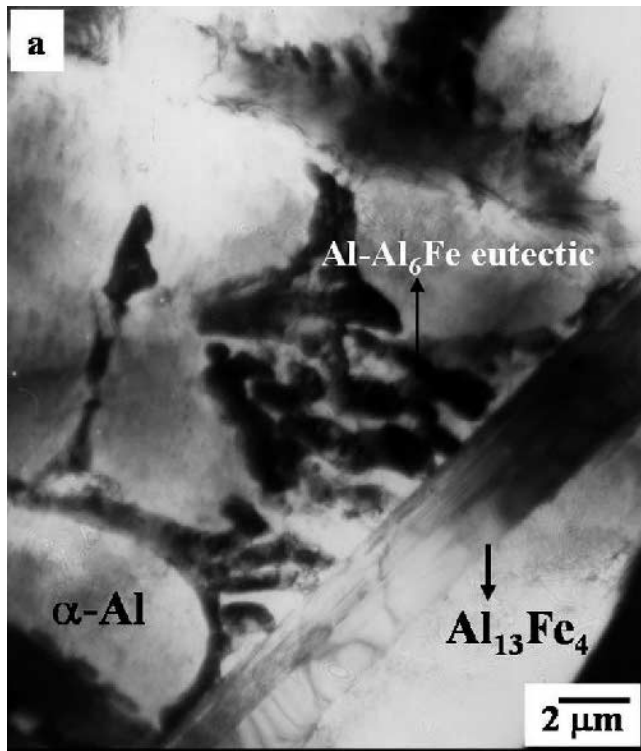


Fig. 3—(a) Low-magnification bright-field image of a region similar to region II, showing different phases, with the inset showing a faulted morphology of $\text{Al}_{13}\text{Fe}_4$. (b), (c), and (d) SADPs taken from different zone axes of $\text{Al}_{13}\text{Fe}_4$. (e) High-magnification image of $\alpha\text{-Al}$, with inset 1 showing the $[112]$ zone axis of aluminum and inset 2 showing the ring pattern of Bi.

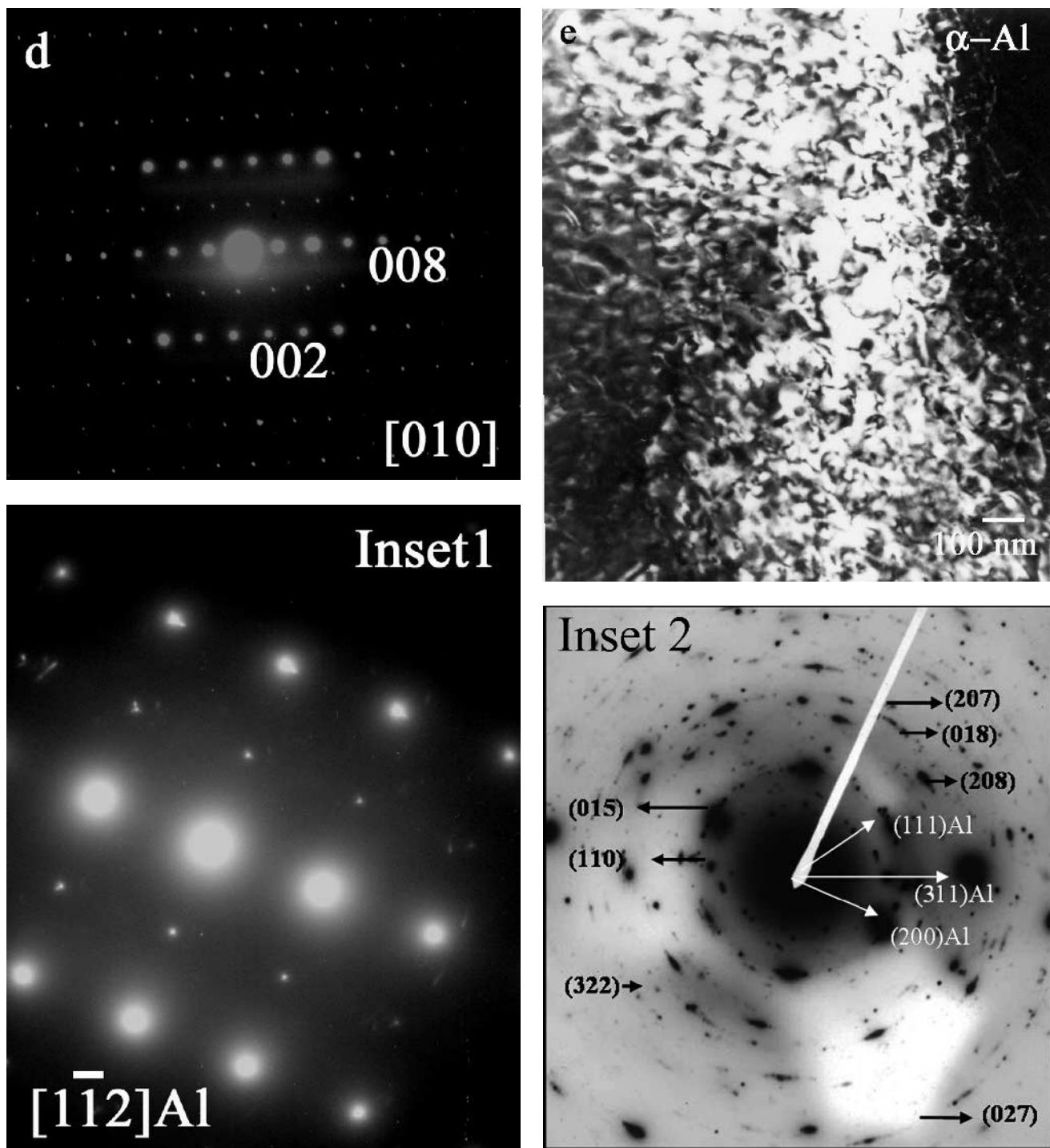


Fig. 3 (Continued)—(a) Low-magnification bright-field image of a region similar to region II, showing different phases, with the inset showing a faulted morphology of $\text{Al}_{13}\text{Fe}_4$ (b), (c), and (d) SADPs taken from different zone axes of $\text{Al}_{13}\text{Fe}_4$. (e) High-magnification image of $\alpha\text{-Al}$, with inset 1 showing the $[112]$ zone axis of aluminum and inset 2 showing the ring pattern of Bi.

monoclinic phase having the lattice parameters $a = 1.55$ nm, $b = 0.807$ nm, and $c = 1.25$ nm and $\beta = 107.731$ deg. Three representative major zone axes from this plate, revealing monoclinic characteristics, are shown in Figures 3(b) through (d). The dendritic phase that exists in between the plates is found to be a solid solution of aluminum. This phase exhibits strain contrast. The higher-magnification micrograph of $\alpha\text{-Al}$ is shown in Figure 3(e). These regions contain a very-fine-scale

dispersion of Bi particles. The two insets of Figure 3(e) show the SADP of aluminum and diffraction rings of randomly distributed Bi. The microstructure of the region between the plates and $\alpha\text{-Al}$ indicates the presence of a eutectic. The eutectic is more prominent in the remelted samples. The observed microstructure is identical in both the as-clad and the remelted samples, and, for conservation of space, we have presented the details in the section on remelted samples.

Figure 4(a) shows a low-magnification bright-field micrograph of region III (similar to Figure 1(a)). The microstructure shows the presence of three different structural features,

as marked in the figure. These are the 1/1 cubic rational approximant, α -Al, and a degenerate Al-Al₂Cu eutectic. The approximant phase (a crystalline phase closely related to

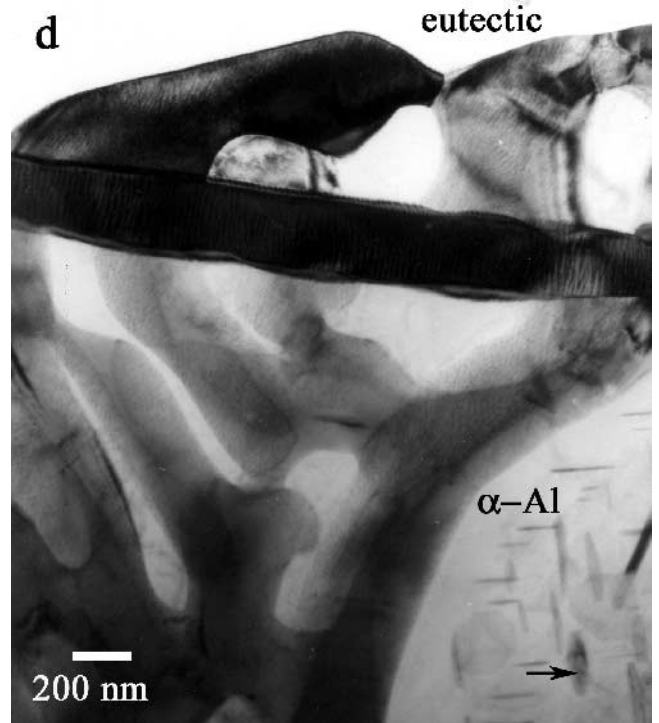
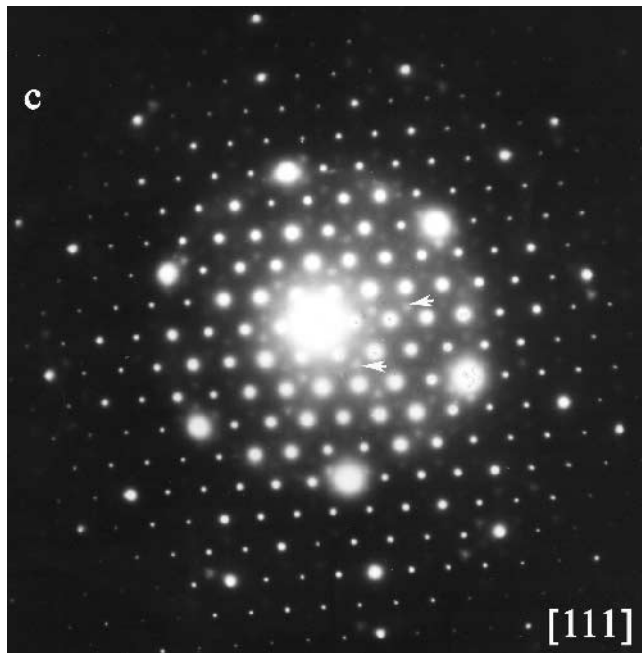
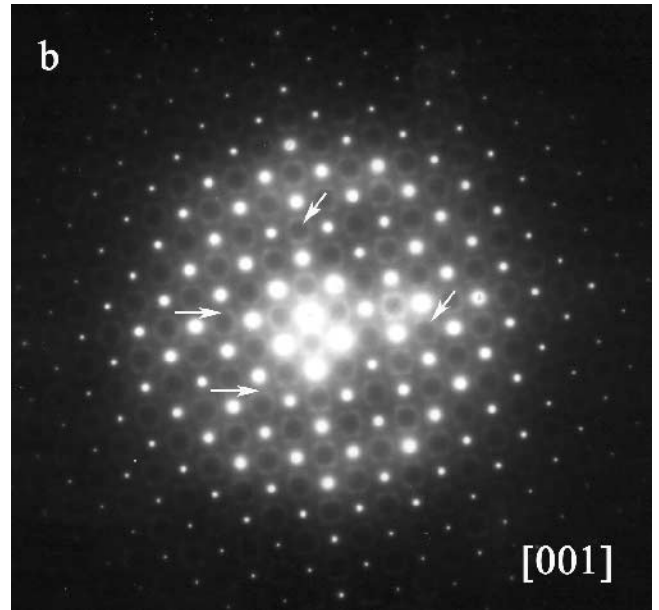
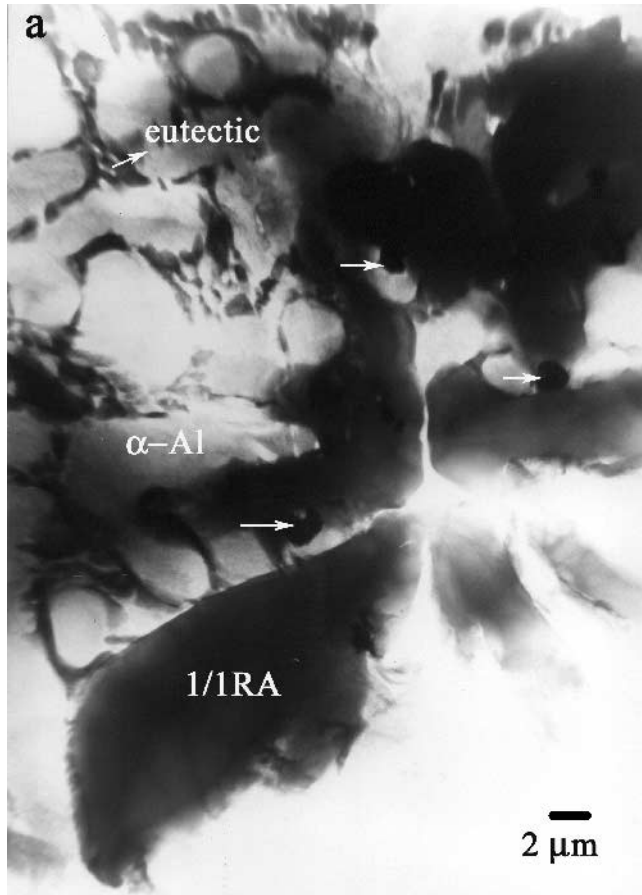


Fig. 4—(a) Low-magnification bright-field image of a region similar to region III (Fig. 1(a)) showing different phases as marked on the figure. (b) and (c) SADPs along the [001] and [111] axes, respectively, taken from the 1/1 rational approximant. (d) A higher-magnification bright-field image of degenerative Al-CuAl₂ eutectic, with the inset showing a microdiffraction pattern taken along the [012] direction of CuAl₂. The black arrows indicate the presence of precipitates in α -Al. The white arrows in (a) indicate holes, which may have been created due to falling off of bismuth particles during ion milling.

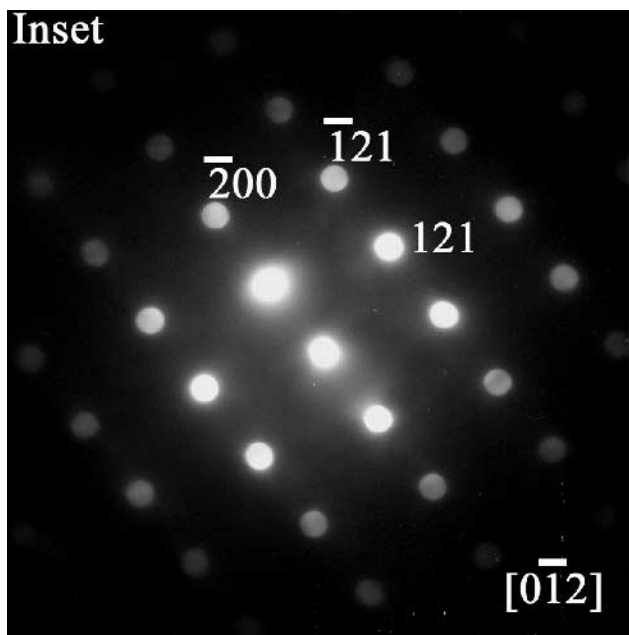


Fig. 4 (Continued)—(a) Low-magnification bright-field image of a region similar to region III (Fig. 1(a)) showing different phases as marked on the figure. (b) and (c) SADPs along the [001] and [111] axes, respectively, taken from the 1/1 rational approximant. (d) A higher-magnification bright-field image of degenerative Al-CuAl₂ eutectic, with the inset showing a microdiffraction pattern taken along the [012] direction of CuAl₂. The black arrows indicate the presence of precipitates in α -Al. The white arrows in (a) indicate holes, which may have been created due to falling off of bismuth particles during ion milling.

quasi-crystals^[14] has a rounded morphology with arms radiating from the central core (Figure 4(a)). The SADPs taken from one of the arms of the approximant phase along the [100] and [111] zone axes are shown in Figures 4(b) and (c), respectively. One can find that the SADPs show the presence of strong diffuse scattering, which is marked by white arrows in Figures 4(c) and (d). The origin of this diffuse scattering is under study. The higher-magnification micrograph of the eutectic is shown in Figure 4(d). This micrograph clearly shows the degenerate nature of the eutectic. It consists of α -Al and a CuAl₂ intermetallic phase. The microdiffraction pattern taken along the [012] axis from CuAl₂ is shown in the inset. One can also observe that α -Al regions containing precipitates (black arrow in Figure 4(d)).

B. Characterization of the Clad and Remelted Sample

We shall now present the results of the clad sample remelted with a scan speed of 500 mm/min. The processing was done in a preprogrammed consecutive pass involving cladding and remelting. The X-ray diffraction pattern of the top surface indicates the coexistence of similar phases to those observed for the as-clad samples.

Figure 5(a) shows a low-magnification optical micrograph of half of the cross section of the remelted layer. Analogous to the as-clad layer, the remelted layer consists of three distinct microstructural layers, labeled as I, II, and III. The composition analysis of the remelted layer (Figure 5(b)) shows the distribution of elemental compositions across the regions. The composition profiles of the remelted track are different, particularly in region II compared to the as-

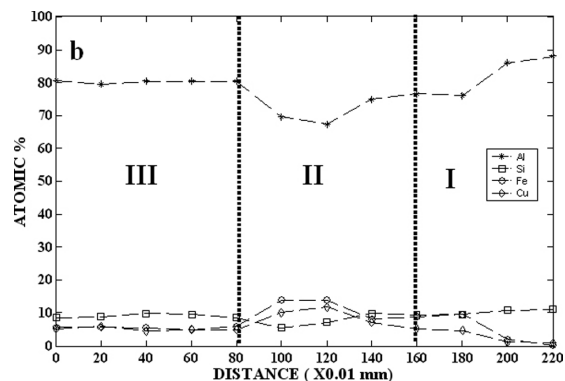
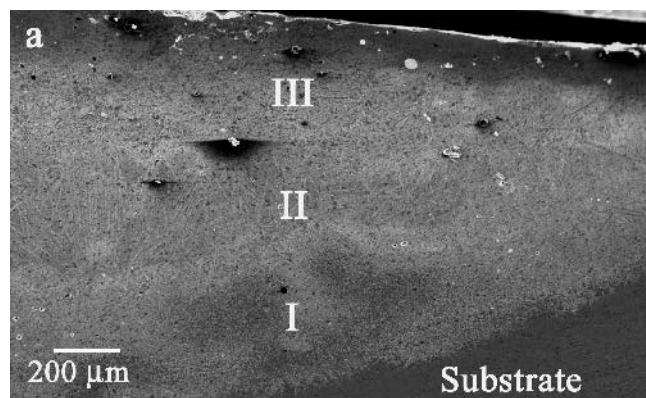


Fig. 5—(a) Low-magnification optical micrograph of half of a cross section of a remelted (500 mm/min) track, showing three different microstructural regions labeled as I, II, and III. (b) Composition profiles showing the variation of elemental composition as a function of distance.

clad track. Near the clad/substrate interface (region I), the aluminum content (~ 80 at. pct) is quite high. The copper content is on the higher side (>10 at. pct) compared to the iron content. The silicon content is found to be at an almost constant level of 8 at. pct. In layer II, the aluminum content decreases to 70 at. pct. There is a substantial increase of iron content (~ 15 at. pct) and a dip in silicon content (7 at. pct) in this layer. The top layer (III) shows a substantial increase in aluminum content (~ 75 at. pct). The iron content shows a drop compared to layer II, while the silicon content remains at about 10 at. pct. The copper content remains at 10 at. pct.

Figure 6 shows SEM micrographs of different regions of the remelted track. Figure 6(a) shows a high-magnification BSE micrograph of the region marked I in Figure 5(a). This micrograph shows the presence of primary aluminum (α -Al), a blocky phase (B), lamellar eutectic (termed eutectic), and bismuth. The phases and their morphologies are similar to those observed for the as-clad track (Figure 2(a)). The faceted growth morphology of the blocky phase is again highlighted by marking six faces of one such particle in the micrograph. The nature of the eutectic (ternary eutectic consisting of α -Al, Si, and Al₂Cu) is identical to that discussed in the case of the as-clad layer.

The microstructure of region II is shown in Figure 6(b). Four different microstructural features characterize this region. The long plates are found to be (Al,Cu)₁₃Fe₄ (EDS shows a composition of Al₇₄Cu₄Fe₂₂). A different phase can be seen growing from the surface of these plates. The EDS

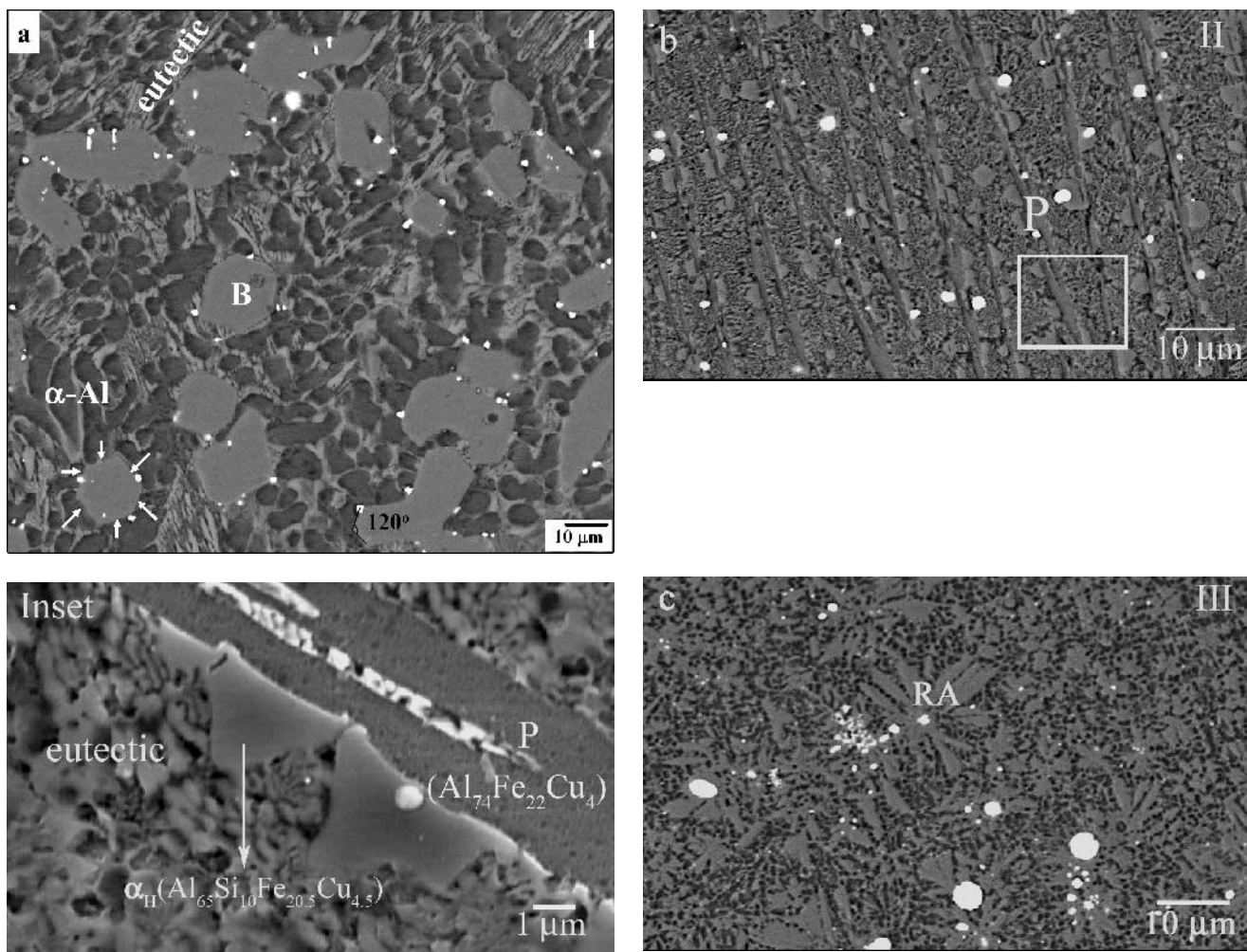


Fig. 6—(a) BSE image of a different region labeled I in Fig. 5(a), showing phases similar to those of the as-clad track: blocky (B phase) α_H -AlFeSi, α -Al, and a ternary eutectic consisting of CuAl_2 , α -Al, and Si. Blocky phases are faceted. Facets of one such crystal are marked by white arrows. One can also find that the angle extended by two faces is about 120 deg. (b) BSE image of a different region labeled II in Fig. 5(a). The inset shows a higher-magnification image of the region marked in the figure. (c) BSE image of a region similar to region III in Fig. 5(a), showing a large number of 1/1 cubic rational approximant phase particles.

analysis shows a composition of $\text{Al}_{65}\text{Si}_{10}\text{Fe}_{20}\text{Cu}_5$ for this phase. This indicates that the composition of this phase is similar to the hexagonal α_H -AlFeSi reported in the literature.^[13] A similar type of microstructural feature has been observed in the case of the as-clad track. The aforementioned phases coexist with a eutectic region. The higher-magnification micrograph of the eutectic is shown in the inset of Figure 6(b). A degenerative eutectic morphology can be observed. The fourth phase (bright contrast) that can be observed in the microstructure is bismuth.

The higher-magnification BSE micrograph taken from region III (as shown in Figure 5(a)) is shown in Figure 6(c). It shows a microstructure consisting predominantly of star-like dendrites. The average composition of these dendrites is found to be $\text{Al}_{66}\text{Si}_9\text{Fe}_{15}\text{Cu}_{10}$. One can also find a substantial amount of bismuth particles.

In order to obtain the structural information of different phases, we have carried out a TEM examination of regions II and III of the remelted sample. The low-magnification image of an area from region II in Figure 5(a) is shown in Figure 7(a). It reveals the presence of a phase with a long, plate-

shaped morphology, α -Al, and a eutectic. The plate-shaped phase is similar to the one shown for the as-clad track (Figure 3(a)). This phase is found to be heavily faulted. The SADPs establish this phase to be monoclinic, again, similar to that observed in the case of the as-clad track. Figures 7(b) and (c) show a bright-field/dark-field pair revealing one of the coexisting phases of the eutectic. The corresponding diffraction pattern (Figure 7(d)) and other similar patterns establish the phase to be Al_6Fe with the following lattice parameters: $a = 0.7464$ nm, $b = 0.6441$ nm, and $c = 0.8786$ nm. The SADPs indicate the other phase of the eutectic to be α -Al.

Figure 8 shows the presence of an additional phase growing at the interfaces of the $\text{Al}_{13}\text{Fe}_4$ plates. The bright-field image is shown in Figure 8(a). The microdiffraction patterns taken from this phase establish its structure to be hexagonal α_H -AlFeSi with $a = 1.2404$ nm and $c = 2.6234$ nm. A typical microdiffraction pattern taken along the $[\bar{1}2\bar{1}3]$ zone axis is shown in Figure 8(b). The α -Al phase marked in Figure 8(a) exhibits strain contrast. The diffraction studies (not shown here) indicate the presence of binary precipitates of θ' and θ plates within this phase.

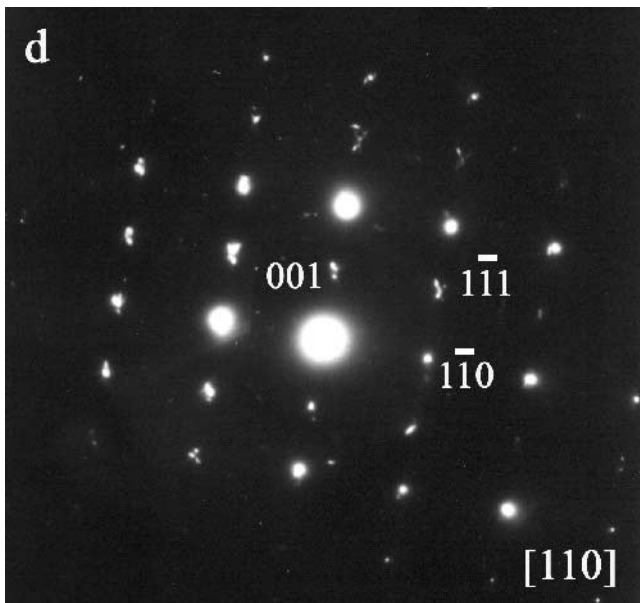
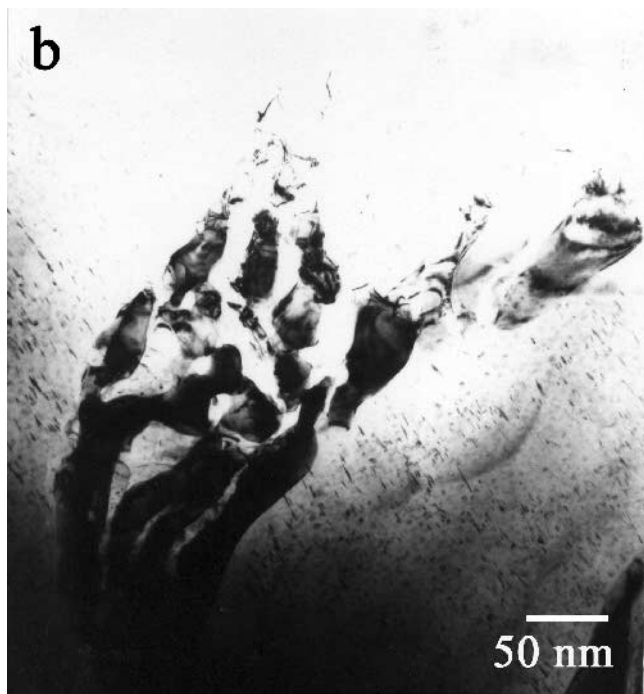
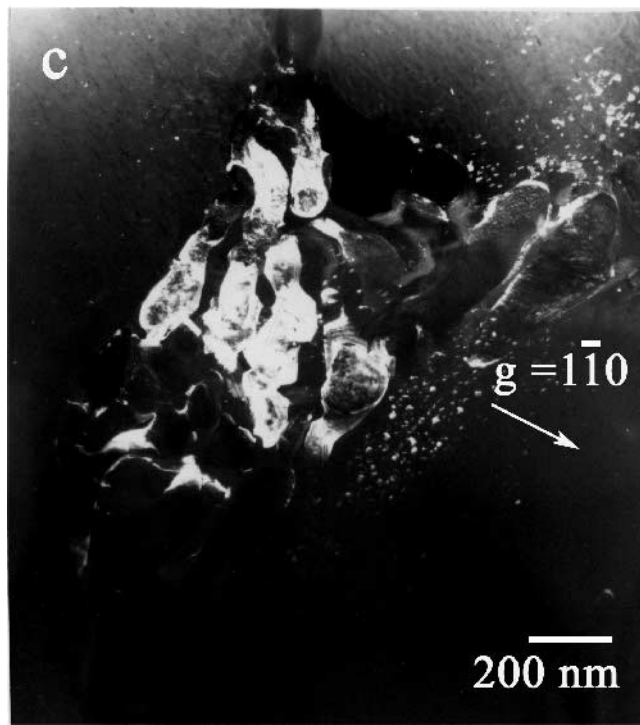
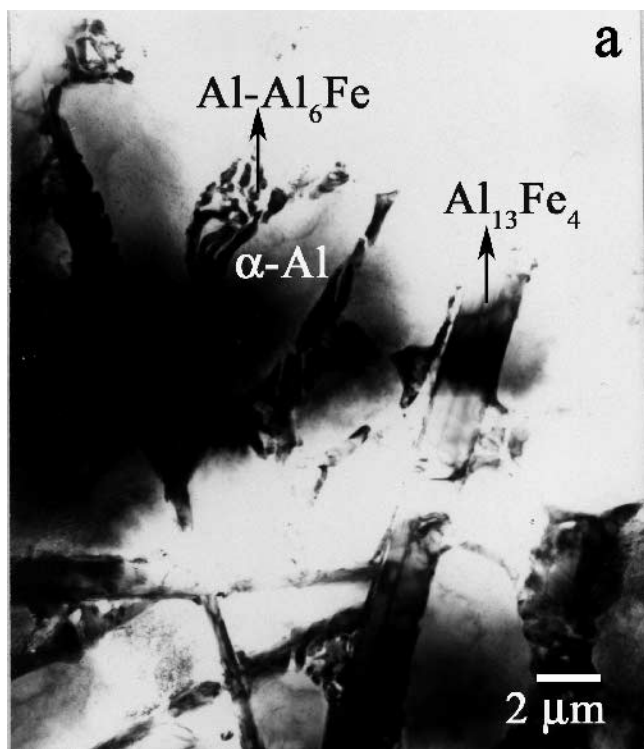


Fig. 7—(a) Low-magnification-bright field image of area containing plate-shaped $\text{Al}_{13}\text{Fe}_4$ and lamellar $\text{Al}-\text{Al}_6\text{Fe}$ eutectic. (b) Higher-magnification bright-field image of metastable $\text{Al}-\text{Al}_6\text{Fe}$ eutectic. (c) Dark-field image taken with $g = [110]$ lighting up Al_6Fe lamellae. (d) a $[110]$ zone-axis pattern of Al_6Fe .

The low-magnification image taken from an area similar to region III in Figure 6(c) is shown in Figure 9(a). The microstructure consists of a $1/1$ cubic rational approximant phase (the radiating dendrites) and $\alpha\text{-Al}$. This is consistent with the SEM micrograph of the top layer of the remelted track. The diffraction patterns taken along the $[001]$, $[101]$, and $[11\bar{1}]$ zone axes are shown in Figures 9(b) through (d),

respectively. The lattice parameter of this approximant phase can be calculated using the formula given by Elser and Henley.^[14] For any quasi-crystalline approximant of the order p/q , the lattice parameter is given by

$$a_{p/q} = \frac{2(q\tau + p)a_R}{\sqrt{2 + \tau}}$$

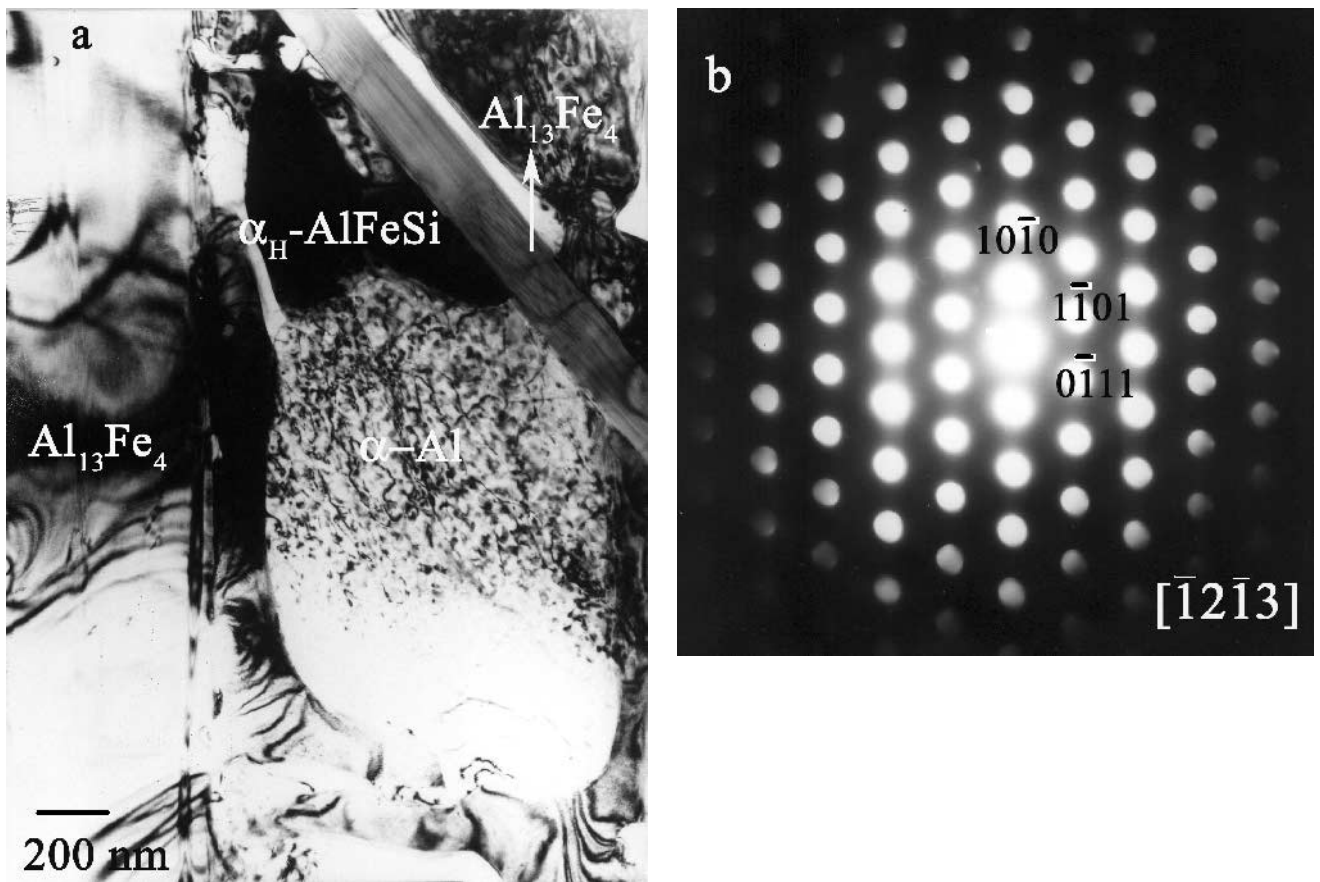


Fig. 8—(a) Bright-field image showing the growth of hexagonal α_H -AlFeSi at the surface of plate-shaped $\text{Al}_{13}\text{Fe}_4$, and (b) a microdiffraction pattern [1213] taken from one such grain of α_H -AlFeSi.

where a_R is the quasi-lattice constant, and τ is the golden mean, given by $(\sqrt{5} + 1)/2$. Therefore, for the 1/1 approximant phase ($p/q = 1/1$), using $a_R = 0.447 \text{ nm}$,^[15] we get $a_{1/1} = 1.23 \text{ nm}$. The estimated value from the diffraction patterns is $1.23 \pm 0.05 \text{ nm}$. This shows a clear match between the experimentally observed value and the theoretically expected value.

C. Hardness and Wear Study

The typical hardness profiles along the cross section of both the as-clad and remelted track (remelted at a scan speed of 500 mm/min) are shown in Figures 10(a) and (b). Figure 10(a) indicates that the hardness is quite high and uniform ($\text{HV}_{0.025} \sim 550$) in the as-clad sample. The hardness drops to a lower value ($\text{HV}_{0.025} \sim 400$) near the coating/substrate interface. For the remelted track (Figure 10(b)), the peak hardness is observed at about the middle of the track ($\text{HV}_{0.025} \sim 600$). The hardness drops to a lower value ($\text{HV}_{0.025} \sim 350$) in the top layer. This is a common characteristic of all the remelted tracks. Therefore, remelting leads to a change in hardness in the top layer. The microstructural studies reported earlier indicate the presence of predominantly the 1/1 rational approximant in this layer. The high hardness in the remelted pool is associated with plate-shaped primary $\text{Al}_{13}\text{Fe}_4$ phase coexisting with the Al- Al_6Fe eutectic.

The typical coefficient-of-friction vs stress plot for the as-clad samples tested in air is shown in Figure 11(a). In all

cases, the coefficient-of-friction values are also reported for the Al-Cu-Fe-Si alloy-clad sample and the Al-10.5 at. pct Si alloy substrate, for comparison. The coefficient-of-friction value (~ 0.21) of the clad sample at a stress level of 1.21 MPa is quite low as compared to the substrate. However, the coefficient-of-friction values are similar to those samples without Bi. A similar plot for the clad sample tested in vacuum is shown in Figure 11(b). Again, the coefficient-of-friction value for Al-Si-Cu-Fe-Bi is quite low (~ 0.2), but not much different from that for Al-Si-Cu-Fe. The coefficient-of-friction values for the clad sample tested in vacuum are slightly lower compared to those for the sample tested in air, although the difference is not significant. Figure 11(c) depicts the wear behavior of the clad sample tested in air. The wear resistance of the Bi-containing clad is better compared to the Al-Si-Cu-Fe clads, and the wear volumes of both of the clad layers are substantially lower as compared to that of the Al-10.5 at. pct Si substrate. The wear characteristics of the clad samples tested in vacuum are shown in Figure 11(d). The Bi-containing clad shows very low wear loss compared to the Al-Si-Cu-Fe alloy clad, which has been used for benchmarking. The effects of remelting on friction and wear behavior are shown in Figures 11(e) and (f). The friction coefficients of the remelted tracks (remelted at 300 and 500 mm/min) tested in air are shown (Figure 11(e)) along with that of the as-clad track for comparison. The friction coefficient of the substrate is higher than that of the as-clad tracks, whereas the friction coefficients of the remelted tracks are

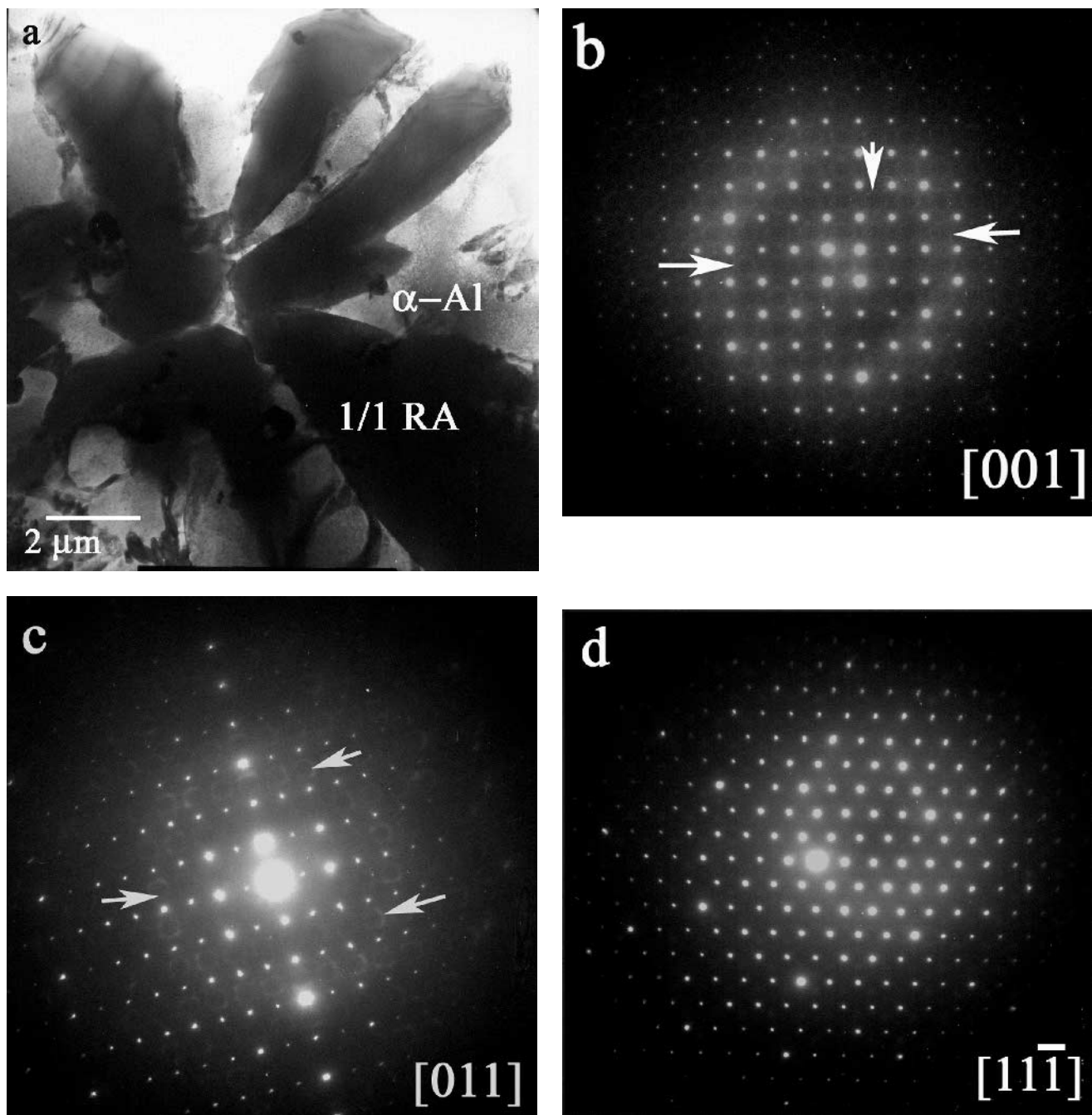


Fig. 9—(a) Bright-field image of the 1/1 cubic rational approximant to the icosahedral phase, and (b) [001], (c) [101], and (d) [111] zone-axis patterns of the phase with $a = 12.33 \text{ \AA}$. The white arrows indicate the position of diffuse intensity maxima in the diffraction patterns.

almost similar. The wear behaviors of all the remelted tracks tested in air are shown in Figure 11(f). The as-clad track shows better wear behavior than the remelted tracks. The wear loss of the tracks remelted at 500 mm/min is higher than that for the tracks remelted at 300 mm/min. Figure 12 shows a secondary electron (SE) image of the worn pin surface of the Bi-containing clad tested in air and vacuum. The SE image (Figures 12(a) and (b)) of worn pin surface of Al-Si-Cu-Fe-Bi clad tested in air at a 0.61 MPa stress level shows the presence of Bi particles (shown by small black arrows) on the wear track. The wear direction is shown by the long white arrow. The wear track shows a large number of sub-

surface deformation marks. The SE image taken from the clad layers tested in vacuum at a stress level of 0.61 MPa is shown in Figure 12(b). One can see Bi particles distributed on the wear tracks (black arrows). The worn surfaces are much smoother in these micrographs as compared to the micrographs for the samples tested in air. The worn pin surfaces of the Al-Si-Cu-Fe (Figures 12(c) and (d)) clad layers show a substantial amount of subsurface deformation and cracks as compared to the worn pin surface of the Bi-containing clad layers. The SE images taken from the Al-Si-Cu-Fe worn pin tested in air at a stress level of 0.61 MPa are shown in Figure 12(c). The presence of cracks and substan-

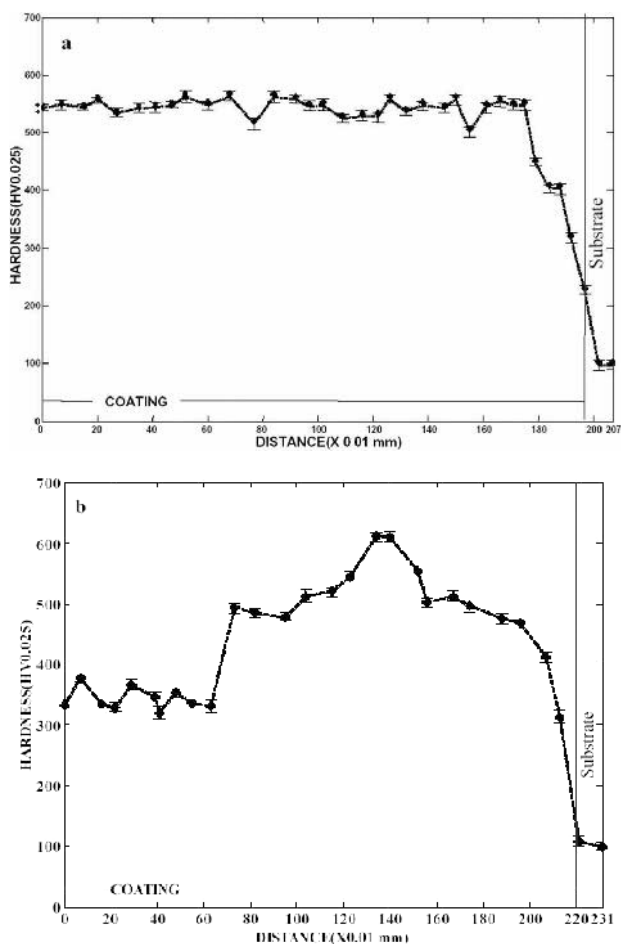


Fig. 10—Microhardness profiles of (a) an as-clad and (b) remelted (500 mm/min) track.

tial subsurface deformation can be seen clearly (indicated by the small white arrow). The SE image taken from the Al-Si-Cu-Fe worn pin surface tested in vacuum at a stress level 0.61 MPa is shown in Figure 12(d). No crack can be seen in this case. The surface is quite smooth as compared to the pin surface tested in air. Figure 13 shows the SE micrographs taken from wear debris of the Bi-containing as-clad track tested at a stress level of 0.61 MPa. The micrograph shows the presence of a large number of bismuth particles in a deformed matrix. The EDS spectrum from one such particle is shown in Figure 13(b). It confirms the presence of bismuth in the debris. The compositional analysis of the debris indicates a matrix composition of $Al_{65}Si_{10}Fe_{20}Cu_5$.

IV. DISCUSSION

The main aim of this investigation is to develop an alloyed surface on an Al-10.5 at. pct Si alloy substrate, which will improve the tribological properties of the surface. The strategy adopted in the present case is to exploit the superior tribological properties of quasi-crystals and related phases in the Al-Cu-Fe system,^[16] together with the dispersion of a soft phase such as Bi. The key to achieving this goal is to develop a suitable phase mixture and microstructures by controlling the process parameters.

We have adopted an elemental powder mixture instead of alloyed powder as feed for the cladding process, followed by remelting to further control the microstructure. In general, the use of an elemental powder mixture containing four components in order to produce a desired microstructure during laser cladding is challenging and requires a systematic effort. The conditions presented here (cladding with select process parameters and a further remelting with a scan speed of 500 mm/min) represent the optimized conditions obtained by us. Our results suggest that we are successful in obtaining a fairly uniform average composition throughout the alloyed layers, except in the areas near the clad/substrate interface, where the concentration of the alloying additions decreases sharply due to dilution by the matrix. However, the results indicate a distinct microstructural gradient in both cases. The evolving microstructure in the surface-alloyed layer can be classified into three zones, primarily on the basis of phases present. Thus, the evolution of microstructures and phase selection (specially in zones II and III) must have been influenced by the prevailing condition of heat transfer during laser processing and the consequent melting and solidification rates as a function of the location across the alloyed layer from the substrate to the top of the surface. The rate of movement of the solid/liquid interface at the top should approach the laser-scan velocity under steady-state conditions, while near the substrate, it should be very low. The growth morphology of a single dendrite/cell from the substrate to the top generally allows estimation of the local growth rate of the solid/liquid interface.^[17] Unfortunately, however, growth of no single dendrite/cell extends from the substrate-alloyed layer to the top. Thus, a quantitative estimate of the growth velocity from the microstructure by measurements of the local angle of the growth axis with the direction of the laser beam^[18] is not possible in the present case. In order to obtain a rough estimate of the prevailing thermal conditions, we have employed a computational approach (developed previously by our group^[19]) to estimate the temperature history at three different locations across the alloyed layers I, II, and III, corresponding to the three microstructural zones. A typical computed temperature history of these three points is shown in Figure 14. The slope of these curves represents the cooling rate in the liquid prior to the intervention of the solidification front. Thus, for a given solidification temperature, the curves in Figure 14 allow us to estimate the prevailing cooling rate in the liquid state prior to the solidification. As can be seen, irrespective of the solidification temperature, the cooling rate is fairly large (10^3 K/s). Thus, one expects significant undercooling of the liquid/solid interface, leading to nonequilibrium solidification. The pathways for such a process, which controls the microstructure evolution, are difficult to estimate for the quaternary alloy.

The phase relations for quasi-crystal-forming ternary Al-Cu-Fe alloys have been extensively studied.^[20,21] These results have been recently utilized to rationalize the phase evolution during laser processing of Al-Cu-Fe alloys on a pure aluminum substrate.^[22] The quasi-crystalline phase in this system can form either directly from the liquid or by a peritectic reaction and coexists with the predominant $Al_{13}Fe_4$ phase. The addition of silicon affects the formation of quasi-crystalline phase. In rapid-solidification experiments involving chill casting and melt spinning, Lee *et al.*^[10] have shown that quasi-crystalline phase cannot form when the Si content is above 5 at. pct. Instead, one observes an approximant phase.

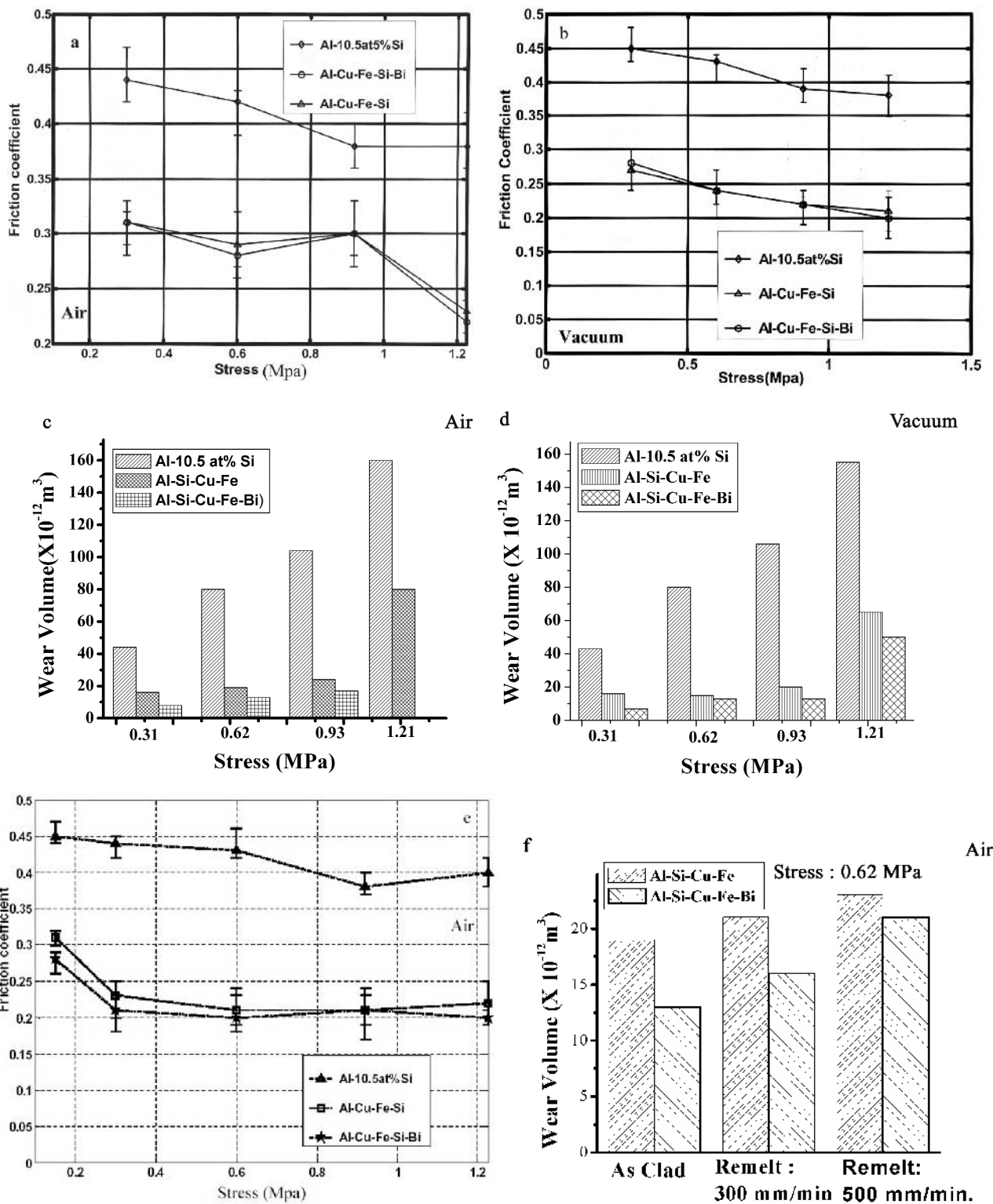


Fig. 11—Friction behavior of the as-clad (300 mm/min) samples: (a) tested in air and (b) tested in vacuum. Wear behavior of the as-clad sample shown as a wear volume vs stress plot: (c) tested in air and (d) tested in vacuum. Friction behavior (e) and wear behavior (f) of the remelted (500 mm/min) sample tested in air. The friction and wear behavior of Al-Si-Cu-Fe-clad Si and 10.5 at. pct Si are shown for comparison and benchmarking.

Our results indicate that the microstructure near the substrate consists of primary α_H hexagonal phase having a quaternary composition $(Al,Si)_{72}(Cu,Fe)_{28}$. Structurally, this phase is very similar to that reported by Bendersky *et al.*^[13] in a rapidly solidified aluminum-rich Al-Fe-Si alloy. Dur-

ing the growth of this phase, the liquid composition shifts due to partitioning to closer to the composition corresponding to a ternary eutectic composition consisting of α -Al, $CuAl_2$, and Si at the aluminum-rich end. Thus, one observes the coexistence of ternary eutectic together with

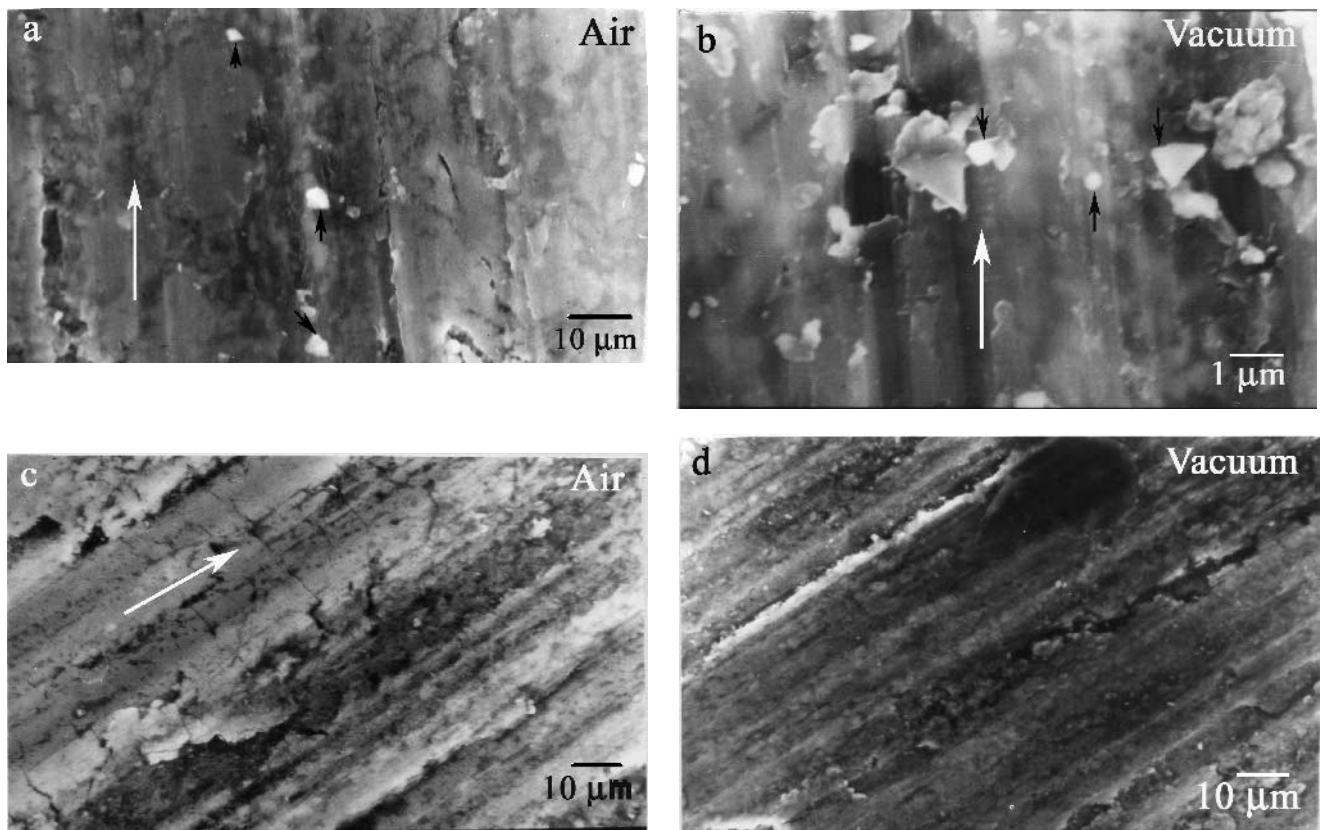


Fig. 12—SEM image of the worn pin surfaces: (a) the as-clad Al-Si-Cu-Fe-Bi sample (300 mm/min) tested in air, (b) the as-clad Al-Si-Cu-Fe-Bi sample (300 mm/min) tested in vacuum, (c) the as-clad Al-Si-Cu-Fe sample (300 mm/min) tested in air, and (d) the as-clad Al-Si-Cu-Fe sample (300 mm/min) tested in vacuum. The white arrows indicate the wear direction and the black arrows indicate the Bi particles.

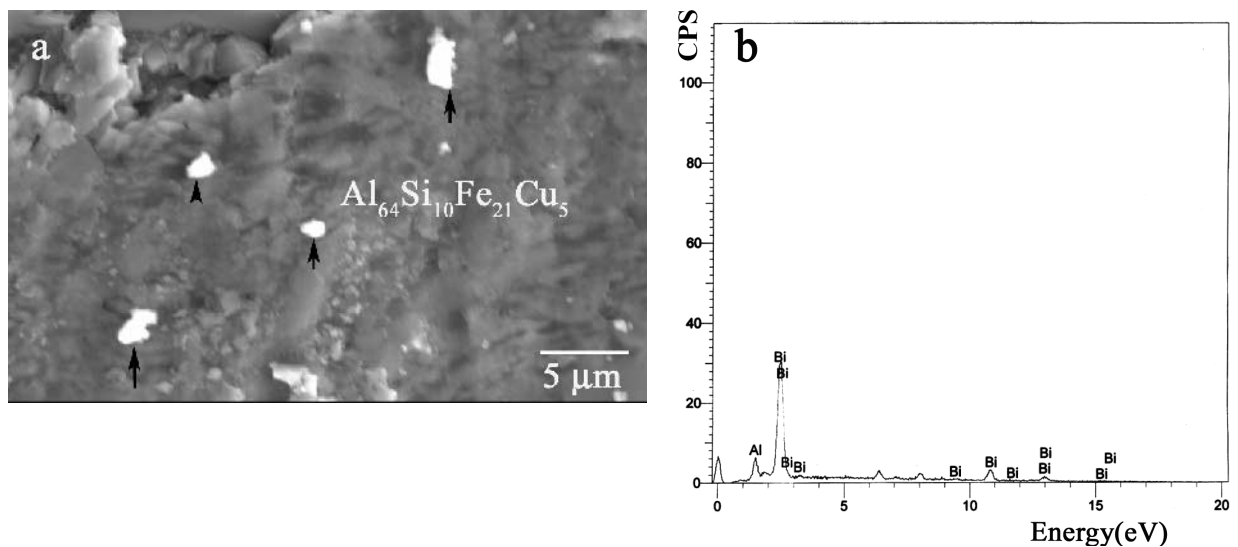


Fig. 13—(a) SE micrograph of the debris from the Bi-containing clad after the wear test, and (b) EDS image taken from one such Bi particle, confirming the presence of Bi in wear debris. The black arrows in Figure 13(a) indicate bismuth.

a smaller amount of α -Al primary phase. Significantly, the Bi particles, which separate in the liquid during solidification, are pushed toward the α_H - phase interface and decorate this interface.

The intermetallic $Al_{13}Fe_4$ phase nucleates away from the substrate/clad-layer interface and dominates the microstructure

of the middle region (zone II). It grows with a plate-shaped morphology with a characteristic faulted morphology, which can be revealed by TEM observations. The tilting experiments revealed that the faults are on the (001) plane (refer to the streaks in the inset of Figure 3). Our observation is consistent with the $1/2[100]$ stacking faults reported during growth

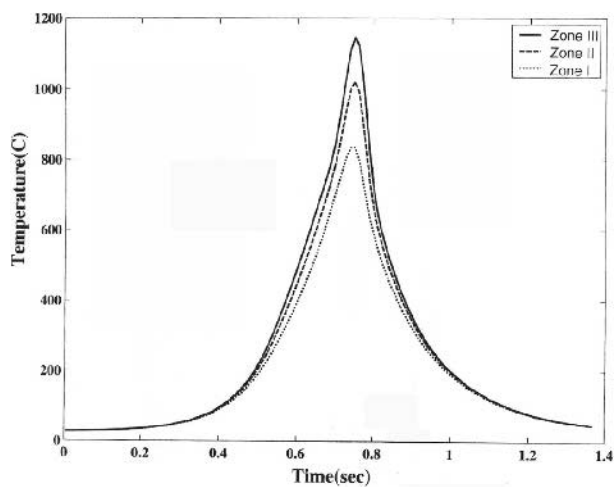


Fig. 14—Computed temperature history of three points similar to the three zones of the as-clad track.

of this phase.^[23] The density of this phase in the remelted layer is comparatively higher. Microstructural observations suggest that remelting with a laser-scan speed of 500 mm/min does not melt the clad layer completely, and the pre-existing $\text{Al}_{13}\text{Fe}_4$ phase acts as a site for renucleation and growth of this phase at the higher velocity imposed by the higher scan speed. Our results (not shown here) also indicate twin-related branching of the plates toward the top of the layer. This result is consistent with results reported earlier,^[24] pointing to a tendency of twinning at a higher growth rate.

The top layer (zone III) in both the as-clad sample and the remelted sample (which experiences both the highest cooling rate and growth rate) is characterized by the presence of a 1/1 cubic rational approximant phase of quasi-crystals. This phase exhibits a free dendritic growth morphology with near-five-fold dendritic arms. This can be compared with our earlier results of cladding of Al-Cu-Fe on a pure aluminum substrate,^[25] where the quasi-crystalline phase forms in the top layer. Clearly, the Si addition had promoted the formation of the approximant phase, and this result is consistent with other reports.^[10,11] The $\text{Al}_{13}\text{Fe}_4$ plates, in small amounts, could only be seen in zone III in the as-clad layers, while the remelted samples show the presence of approximant phase coexisting with a small amount of Al- Al_2Cu eutectic, suggesting partitioning of copper during the growth of the approximant phase.

The average compositions across the surface-alloyed layer in zones II and III exhibit no significant change. Therefore, we attribute the formation of approximant phase to the high undercooling achieved in the top layer. This conclusion is supported by the following observations: (1) an unconstrained equiaxed-growth morphology of the approximant phase with growth occurring in all directions and (2) a large number of randomly distributed particles of this phase, suggesting independent nucleation in the undercooled melt.

We note that the Bi particles are predominantly distributed near the primary intermetallic phases. Some of the particles have larger sizes, probably due to coalescence due to convective flow in the liquid. The problem of incorporation of foreign particles in the melt by the growing interface has been analyzed by Uhlmann *et al.*^[26] It is seen that incorporation of smaller particles requires a higher growth velocity. Our results suggest that the most of the Bi parti-

cles separated from the liquid are pushed at the interface, leading to the decoration of the interface. This influences the mechanical properties, which will be discussed next.

The quasi-crystals and related phases are reported to have superior frictional properties.^[16] However, due to the lack of dislocation activity at lower temperatures, they show a brittle behavior and a low fracture-toughness value. The fracture toughness of the Al-Cu-Fe quasi-crystalline coating is reported to be $1.32 \text{ MPa}\sqrt{\text{m}}$,^[25] while the value of the bulk quasi-crystalline single-phase alloy is $1.51 \text{ MPa}\sqrt{\text{m}}$.^[27] One of the primary aims of the present investigation is to evaluate whether the presence of a dispersed soft phase such as Bi further improves the tribological properties as well as the fracture behavior. The latter is reflected in the wear rate. The expectation derives from our recent work, which showed that dispersed nanoscale Pb particles in an aluminum matrix dramatically reduce the coefficient of friction.^[28]

According to the results obtained in this investigation, the dispersion of Bi particles in the clad layer does not affect the coefficient of friction (measured against steel) under dry-sliding-wear conditions. Both the coatings of the Al-Cu-Fe surface alloyed with or without Bi exhibit a low coefficient of friction. We note the presence of a large amount of approximant phase in the zone III region of the both the as-clad and remelted samples. Thus, the present result is consistent with the fact that not only the quasi-crystal phase^[3] but also the related approximant phases exhibit a significantly lower coefficient of friction. Our results on the wear behavior, however, indicate the predominance of a plowing process in all samples.

The following observations need to be kept in mind in order to understand the mechanisms of the wear process. The cracks are observed in the worn surface around the plowing track (Figures 12(a) and (c)). The Bi-containing samples show a significant reduction in the number of cracks. The cracks are more clearly observed in $\text{Al}_{13}\text{Fe}_4$ plates (Figure 15(a)) in the as-clad samples, compared to the remelted samples containing predominantly a cubic approximant phase. The wear rate in the latter case is slightly higher.

The size of the fraction of Bi particles increases during the process of wear. Most of these particles are located near $\text{Al}_{13}\text{Fe}_4$ plates or the approximant phases. The smaller particles decorating these interfaces prior to wear experiments are replaced by a lesser number of bigger particles after the wear. The original Bi particles before the process of wear had a round shape. The increase in size is often associated with a change in aspect ratio of the particles. We have carried out a statistical distribution of this change, covering ~ 100 particles (Figure 16). Two points can be noted. The change in the values of the aspect ratio for smaller particles is small, but the frequency of the occurrences is large. A larger change in the aspect ratio is less frequent and is often associated with bigger particles near the $\text{Al}_{13}\text{Fe}_4$ /approximant phases. The observations of debris also indicate that the transfer layer contains larger Bi particles (Figure 13(a)).

The previous observations allow us to develop an understanding of the wear process in our samples. During the sliding process, the hard phases related to quasi-crystals (approximant and $\text{Al}_{13}\text{Fe}_4$) form the actual contact interface through which load gets transferred. Although this leads to a low coefficient of friction, the brittle nature of these phases leads to wear. Our earlier work had indicated that the Si-containing approximant phase is relatively tougher due to the higher ductility compared

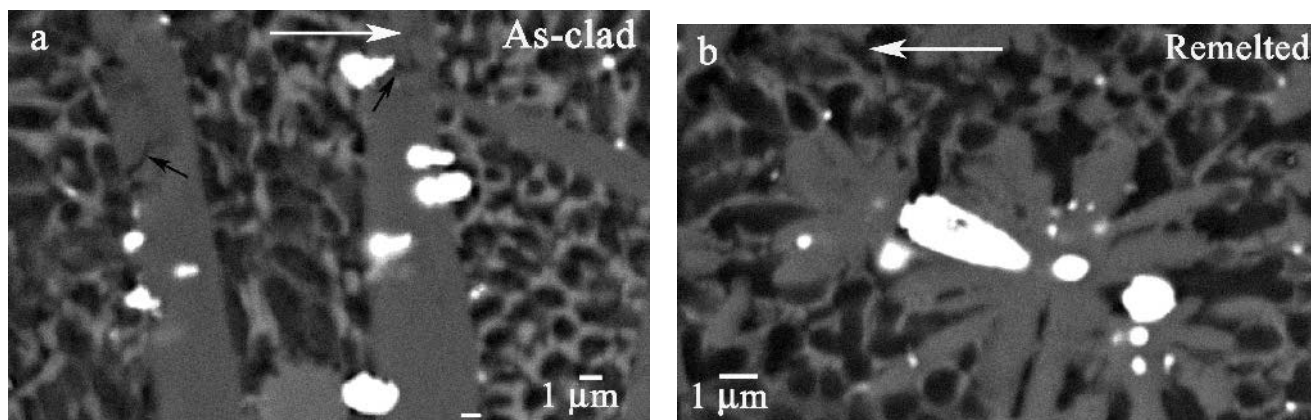


Fig. 15—BSE image of the worn-out pin after etching: (a) the as-clad sample, showing deformed Bi particles along the direction of wear (shown by white arrow). One can find cracks (black arrow) on platelike Al₁₃Fe₄. BSE image of the worn-out pin after etching: (b) the remelted sample, showing deformed Bi particles in the spaces between the arms of the 1/1 cubic rational approximant to the icosahedral quasi-crystal. The white arrow indicates the wear direction.

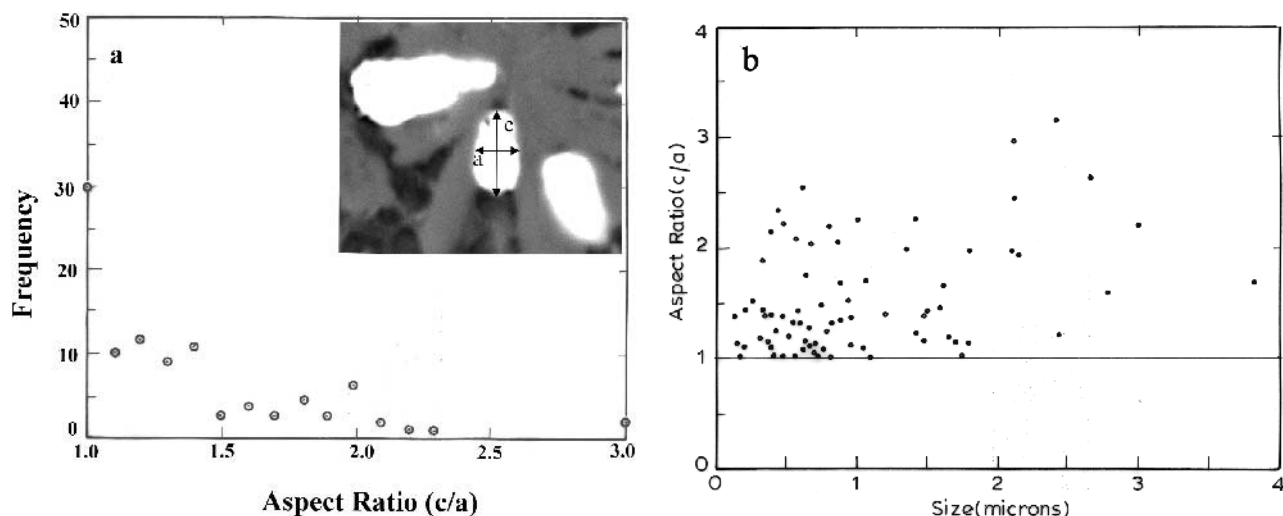


Fig. 16—Plot of (a) frequency vs size and (b) aspect ratio vs size of the deformed Bi particles after the wear test.

to the Al₁₃Fe₄ phase.^[25] Thus, the former phase imparts a higher wear resistance. This is supported by the difference in the observed frequency of cracks in these two phases. The dispersion of Bi clearly imparts a higher wear resistance. The observation of larger particles in transfer layer suggests that these particles play a role in the wear process. As the thermal conductivities of these intermetallic phases are relatively less,^[4] one expects a local temperature rise. This can lead to melting and migration of Bi particles under the influence of sliding-induced stress. This not only leads to coalescence-induced coarsening, but also to a dynamic mechanism to reduce the contact stresses, resulting in improved wear resistance.

V. CONCLUSIONS

We have successfully synthesized by laser processing surface-alloyed layers containing approximant phases of quasi-crystals and other related phases belonging to the Al-Cu-Fe-Si system, containing a fine-scale dispersion of low-melting-point Bi particles on an Al-10.5 at. pct Si substrate. The alloyed layer consists of a microstructure gradient containing a mixture of different phases due to the variation of growth

conditions across the layer during laser processing. The alloyed layer exhibits a lower coefficient of friction. However, the presence of the Bi particles does not influence the frictional behavior. In contrast, the results indicate a clear improvement in wear behavior in samples containing a fine dispersion of Bi particles. Evidence is presented to indicate a direct role of Bi particles during the wear process.

ACKNOWLEDGMENTS

We thank the Council for Scientific and Industrial Research (CSIR, India) and BMBF (Germany) for their assistance in carrying out the present investigation. We also thank Drs. Gandham Phanikumar and Sandip Bysakh for useful discussions. We thank Professor S. Ranganathan for constant encouragement and support.

REFERENCES

1. D. Sheckmann, I. Blech, D. Gratias, and J.W. Cahn: *Phys. Rev. Lett.*, 1984, vol. 53 (20), pp. 1951-53.
2. S.S. Kang and J.M. Dubois: *Phil. Mag. A*, 1992, vol. 66 (1), pp. 151-63.

3. J.M. Dubois, S.S. Kang, and J. von Stebut: *J. Mater. Sci. Lett.*, 1991, vol. 10, pp. 537-41.
4. P. Archambault and C. Janot: *MRS Bull.*, 1997, vol. 22 (11), pp. 48-53.
5. C.J. Jenks and P. Thiel: *MRS Bull.*, 1997, vol. 22 (11), pp. 55-58.
6. J.M. Dubois, S.S. Kang, and Y. Massiani: *J. Non-Crystalline Solids*, 1993, vols. 153-54, pp. 443-45.
7. K. Urban, M. Feuerbacher, and M. Wollgarten: *MRS Bull.*, 1997, vol. 22 (11), pp. 65-68.
8. A.P. Tsai, A. Inoue, and T. Masumoto: *Jpn. J. Appl. Phys.*, 1987, vol. 26 (9), pp. L1505-L1507.
9. J.M. Dubois: in *New Horizons in Quasicrystals (Research and Applications)*, A.I. Goldmann, D.J. Sordet, P.A. Thiel, and J.M. Dubois, eds., World Scientific Publishing, Singapore, 1997, pp. 208-15.
10. S.M. Lee, B.H. Kim, S.H. Kim, E. Fleury, W.T. Kim, and D.H. Kim: *Mater. Sci. Eng. A*, 2000, vols. 294-96, pp. 93-98.
11. A. Quivy, M. Quiquandon, Y. Calvayrac, F. Faudot, D. Gratias, C. Berger, R.A. Brand, V. Simonnet, and F. Hippert: *J. Phys. Condens. Mater.*, 1996, vol. 8, pp. 4223-4334.
12. R. Vilar: *J. Laser Applic.*, 1999, vol. 11 (2), pp. 64-79.
13. L.A. Bendersky, A.J. McAlister, and F.S. Biancaneello: *Metall. Trans. A*, 1988, vol. 19A, pp. 2893-2900.
14. V. Elser and C.L. Henley: *Phys. Rev. Lett.*, 1985, vol. 55 (26), pp. 2883-86.
15. A.P. Tsai, A. Inoue, and T. Masumoto: *J. Mater. Sci. Lett.*, 1989, vol. 8, pp. 470-72.
16. S.S. Kang, J.M. Dubois, and J. von Stebut: *J. Mater. Res.*, 1993, vol. 8 (10), pp. 2471-81.
17. M. Rappaz, G. Gremud, R. Dekumbis, and W. Kurz: in *Laser Treatment of Materials*, Barry L. Mordike, ed., 1987, pp. 43-53.
18. M. Zimmermann, M. Carrad, and W. Kurz: *Acta Metall.*, 1989, vol. 37, pp. 3305-13.
19. S. Sarkar, P. Mohan Raj, S. Chakraborty, G. Phanikumar, K. Chattopadhyay, and P. Dutta: *J. Mater. Sci.*, 2003, vol. 38, pp. 155-64.
20. B. Gruskho, R. Wittenberg, and D. Holland-Moritz: *J. Mater. Res.*, 1996, vol. 11 (9), pp. 2177-85.
21. L. Zhang and R. Lück: *Z. Metallkd.*, 2003, vol. 2, pp. 91-115.
22. K. Biswas, K. Chattopadhyay, R. Galun, and B.L. Mordike: *Mater. Res. Soc. Proc.*, 2004, vol. 805, pp. LL7.1.1-LL7.1.7.
23. Per Skjerpe: *Metall. Trans. A*, 1986, vol. 18A, pp. 189-200.
24. E. Louis, R. Mora, and J. Pastor: *Met. Sci.*, 1980, vol. 14, pp. 591-93.
25. K. Chattopadhyay, K. Biswas, S. Bysakh, G. Phanikumar, A. Weishit, R. Galun, and B.L. Mordike: *Mater. Res. Soc. Proc.*, 2001, vol. 643, pp. K15.3.1-K15.3.12.
26. D.R. Uhlmann, B. Chalmers, and K.A. Jackson: *J. Appl. Phys.*, 1964, vol. 35 (10), pp. 2986-93.
27. U. Köster, H. Liebertz, and W. Liu: *Mater. Sci. Eng.*, 1994, vols. A181-A182, pp. 777-80.
28. V. Bhattacharya and K. Chattopadhyay: *Scripta Mater.*, 2001, vol. 44, pp. 1677-82.